

## Article

# Analysis of the Influence of Shell Sand Content on the Performance of Ceramsite Lightweight Aggregate Concrete

Di Liu <sup>1,2</sup>, Songhui Li <sup>1,2</sup>, Hengxuan Lun <sup>3</sup> and Quanlei Wang <sup>1,2,\*</sup> 

<sup>1</sup> College of Civil Engineering and Architecture, Shandong University of Science and Technology, Qingdao 266590, China

<sup>2</sup> Shandong Provincial Key Laboratory of Civil Engineering Disaster Prevention and Reduction, Qingdao 266590, China

<sup>3</sup> China Construction Eighth Bureau First Construction Co., Ltd., Jinan 250100, China

\* Correspondence: wangql@sdust.edu.cn

**Abstract:** This study investigates the impact of varying shell sand replacement rates (0%, 5%, 10%, 15%, 20%, 25%) on the properties of clay ceramsite lightweight aggregate concrete (CLC) through six experimental groups. Results indicate that a 5% replacement rate of shell sand yields optimal mechanical properties and working performance in CLC. Examination of specimen failure diagrams, electron microscopy and theoretical analysis reveals that shell sand predominantly influences CLC's overall performance by influencing internal pore development and the formation of a “bonding defect zone” between shell sand and cementitious material. This also elucidates why specimen failure predominantly arises from internal ceramic particle fracture.

**Keywords:** shell replacement rate; lightweight aggregate concrete; mechanical properties; microscopic analysis



**Citation:** Liu, D.; Li, S.; Lun, H.; Wang, Q. Analysis of the Influence of Shell Sand Content on the Performance of Ceramsite Lightweight Aggregate Concrete. *Buildings* **2024**, *14*, 986. <https://doi.org/10.3390/buildings14040986>

Academic Editor: Flavio Stochino

Received: 27 February 2024

Revised: 26 March 2024

Accepted: 29 March 2024

Published: 2 April 2024



**Copyright:** © 2024 by the authors. Licensee MDPI, Basel, Switzerland. This article is an open access article distributed under the terms and conditions of the Creative Commons Attribution (CC BY) license (<https://creativecommons.org/licenses/by/4.0/>).

## 1. Introduction

Portland cement concrete is widely used and consumes 50% of the world's raw materials and 40% of the energy [1] and also produces 5% to 8% of global CO<sub>2</sub> emissions [2], which has created serious environmental problems. Compared with traditional concrete, ceramsite lightweight aggregate concrete (CLC) exhibits remarkable attributes, including low density, elevated relative strength, and commendable thermal insulation performance [3]. Considering the defects of Portland cement, researchers found that alkali-activated materials (AAMs) are a potential alternative [4]. Alkali-activated cement has significant advantages over Portland cement, including superior early strength, enhanced durability, lower hydration heat and heightened resistance to chemical erosion [5]. Additionally, to reduce the consumption of river sand in concrete, the researchers found that as an inorganic material with inherent strength, shells can theoretically be used as a partial substitute for river sand after treatment [6]. The influence and change pattern of the replacement rate of shell sand on the mechanical properties and working performance of alkali-induced lightweight aggregate ceramsite concrete is worthy of further research and discussion. This has great social value for its promotion and application in the industry and economic benefits.

Compared with ordinary Portland concrete (OPC), the excellent mechanical properties of alkali-activated concrete (AC) mainly depend on the interface transition zone (ITZ). The ITZ of AC has relatively fewer pores and higher density [7–9] and ITZ products are not coarse calcium hydroxide and quartz crystal, but denser aluminosilicate gel [10,11]. Different mineral admixtures will generate different types of gels during the reaction process. The reaction product of fly ash is mainly N-A-S-H gel [12], and the reaction product of slag is mainly C-A-S-H gel [13]. Both of these have stable properties and a three-dimensional structure for long-lasting performance [14].

On the macro level, researchers found that different mineral admixtures have different effects on concrete properties. Zhang [15] and Cao's [16] results show that compared to kaolin and fly ash, slag demonstrates superior activity, reaction rate, and intensity development characteristics. Dai [17] and Wang [18] found that different alkali dosages have different effects on the properties of AC. Other research [19–21] further indicated that when the water glass modulus is in the range of 1.0–1.4 and the water–cement ratio (W/C) is maintained in the range of 0.30–0.40, the mechanical properties of AC reach the best state. Predecessors have performed a lot of mature research on the performance and dosage of alkali excitation in ordinary concrete, and whether alkali-activated cement can show the same good performance in CLC as in traditional concrete has become the focus of this paper. Çelik et al. [22–27] found that the strength, workability, setting time and environmental properties of geopolymer concrete (GPC) can be effectively improved by using micro-silicon powder as a binder and introducing lathe waste, replacing fly ash with an appropriate amount of waste basalt powder and adding glass fiber. At the same time, the possibility of reducing the consumption of Portland cement by producing various building materials such as gypsum, grout and concrete from the ground raw pearl soil and the influence of the concentration of NaOH and the proportion of waste glass aggregate (WGA) on the performance of geopolymer concrete (GPC) are also explored, which plays a positive role in the research and development of alkali-excited concrete.

Olivia [28] and Bamigboye [29] found that CaO contributes to the bonding interface between the aggregate and cement paste. Ismail [30] found that during alkali excitation, part of the  $\text{Ca}^{2+}$  released by the dissolution of slag can be integrated into the N-A-S-H gel to form an N-C-A-S-H gel with higher bonding strength. Shells contain a large amount of  $\text{Ca}^{2+}$ , which can promote the generation of more N-C-A-S-H gel. This provides another theoretical support for shell sand to partially replace river sand as fine aggregate. Due to the structural differences and different connection properties with cementitious materials between shell sand and river sand, the optimal replacement rate of shell sand in concrete has become the focus of current research. Hasnoy [31] observed that a shell sand replacement rate below 30% leads to higher strength in geopolymer concrete. Researchers have pointed out [32–35] that a shell sand replacement rate of approximately 5% can achieve the best performance of ordinary Portland concrete. Therefore, the influence of the content of shell sand on the properties of CLC has become another focus of this paper.

Mechanical properties of concrete, such as elastic modulus, strength, ductility, shrinkage and fracture properties, depend largely on the material structure at the microscopic scale. The pore structure is an important part of the concrete microstructure, which greatly affects the strength, deformation performance, durability and other properties [36,37]. The current methods for studying pore structure mainly include the mercury intrusion method, the optical method, the X-ray small angle scattering method and the isothermal adsorption method [38]. Since different pore sizes have different effects on the properties of concrete, Zhang [39] divided the pores in concrete into four categories as follows: harmless pores (<20 nm), less harmful pores (20–50 nm), harmful pores (50–200 nm) and hazardous pores (>200 nm). Mehta [40] believed that increasing the proportion of harmless pores and less harmful pores and reducing the proportion of hazardous pores would make the concrete denser and greatly improve the performance of the concrete.

From the perspective of energy conservation and environmental protection, this paper set shell sand (0, 5%, 10%, 15%, 20%, 25%) to replace part of the river sand to prepare the S-CLC control experiment, studied its performance variation rule and further modified the relevant fitting formula to provide reference and suggestions for site construction. At the same time, from the failure phenomenon of the specimen, microscopic electron microscope observation and microscopic theoretical analysis, the influence mechanism is deeply studied and the failure mechanism of the specimen is revealed to promote the further development of light aggregate concrete in the construction field.

## 2. Experimental Program

### 2.1. Materials

#### 2.1.1. Aggregate

In this experiment, clay ceramsite was chosen as the coarse aggregate, adhering to the standards outlined in “Lightweight Aggregate and Test Methods Part 1: Lightweight Aggregate” (GB/T17431.1-2010). The fine aggregates are river sand and shell sand, which meet the specifications specified in the “Standards for Test Methods” (JGJ52-2006), and their specific parameters are shown in Table 1.

**Table 1.** Performance parameters of aggregate.

| Type           | Particle Size (mm) | Packing Density (kg/m <sup>3</sup> ) | Apparent Density (kg/m <sup>3</sup> ) | 1 h WAR (%) | CCS (MPa) |
|----------------|--------------------|--------------------------------------|---------------------------------------|-------------|-----------|
| Clay ceramsite | 5–12               | 622                                  | 730                                   | 6.8         | 3.9       |
| River sand     | 0.15–4.75          | 1560                                 | 2650                                  | \           | \         |
| Shell sand     | 0.15–4.75          | 1220                                 | 2340                                  | \           | \         |

Note: WAR means water absorption rate and CCS means cylinder compressive strength.

#### 2.1.2. Concrete Admixtures

S95 slag with a density of 4200 kg/m<sup>3</sup> was selected as the cementitious material and the performance indexes are shown in Table 2. The alkali activator was prepared by mixing the configured NaOH (concentration is 8 mol/L) solution with the Na<sub>2</sub>SiO<sub>3</sub> solution with a modulus of 3.34 at the ratio of 1:2.5. Additionally, water-reducing agent (Water RES) was added to ensure the workability of the concrete, and the water was sourced from the laboratory of Shandong University of Science and Technology. The other materials in this experiment are shown in Figure 1.

**Table 2.** S95 mineral powder performance Index.

| Specific Surface Area (m <sup>2</sup> /kg) | Density (g/cm <sup>3</sup> ) | CaO (%) | SiO <sub>2</sub> (%) | Al <sub>2</sub> O <sub>3</sub> (%) | MgO (%) | Fe <sub>2</sub> O <sub>3</sub> (%) | SO <sub>3</sub> (%) | Others |
|--|------------------------------|---------|----------------------|------------------------------------|---------|------------------------------------|---------------------|--------|
| 2.9  | 4.2                          | 40.03   | 33.75                | 13.21                              | 9.46    | 0.58                               | 1.04                | 1.93   |

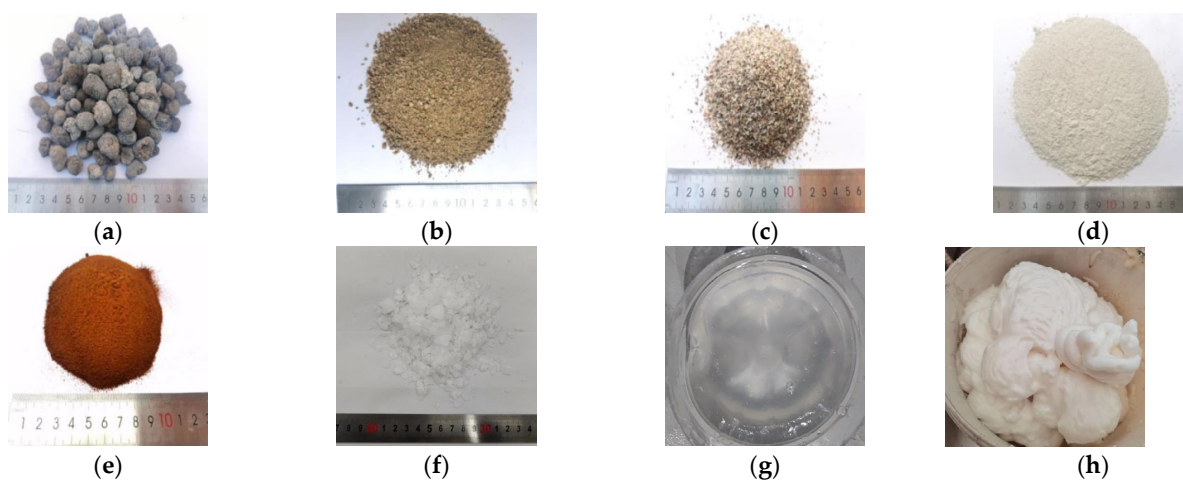


**Figure 1.** Experiment materials: (a) ceramsite; (b) river sand; (c) shell sand; (d) slag; (e) Water RES; (f) sodium hydroxide solid; (g) water glass solution; (h) foam.

## 2.2. Specimens Preparation and Mix Design

The relevant information of the mixing ratio of specimens in this paper is shown in Table 3. All specimens meet the criteria specified in the Technical Standard for the Application of Lightweight Aggregate Concrete (JGJ/T12-2019).

Table 3. The mix ratio design.

| Group | W/C | Ceramsite (kg/m <sup>3</sup> ) | River Sand (kg/m <sup>3</sup> ) | Shell Sand (kg/m <sup>3</sup> ) | Slag (kg/m <sup>3</sup> ) | NaOH (kg/m <sup>3</sup> ) | Water Glass (kg/m <sup>3</sup> ) | Water (kg/m <sup>3</sup> ) | Water RES (kg/m <sup>3</sup> ) |
|-------|-----|--------------------------------|---------------------------------|---------------------------------|---------------------------|---------------------------|----------------------------------|----------------------------|--------------------------------|
| S0    |     |                                | 846.6                           | 0                               |                           |                           |                                  |                            |                                |
| S5    |     |                                | 804.3                           | 42.3                            |                           |                           |                                  |                            |                                |
| S10   | 0.4 | 457.3                          | 761.9                           | 84.7                            | 520                       | 17.3                      | 170.6                            | 128                        | 0.52                           |
| S15   |     |                                | 719.6                           | 127.0                           |                           |                           |                                  |                            |                                |
| S20   |     |                                | 677.3                           | 169.3                           |                           |                           |                                  |                            |                                |
| S25   |     |                                | 634.9                           | 211.7                           |                           |                           |                                  |                            |                                |

Note: S0 is the control group, which means that the shell sand fine aggregate replacement rate is 0%, and the other groups are the experimental groups, such as S25, which means the replacement rate is 25%.

The specimen size for the compression, splitting tensile, softening coefficient and porosity experiments is 100 mm × 100 mm × 100 mm, and the specimen size for the flexural experiment is 100 mm × 100 mm × 400 mm.

## 2.3. Experimental Methods

According to the “Standards for Test Methods of Physical and Mechanical Properties of Concrete” (GB/T50081-2019), the mechanical experiments were carried out using a TYE-3000B compression testing machine. Figure 2a–c respectively illustrate the loading process of compression, splitting tensile and flexural experiment.

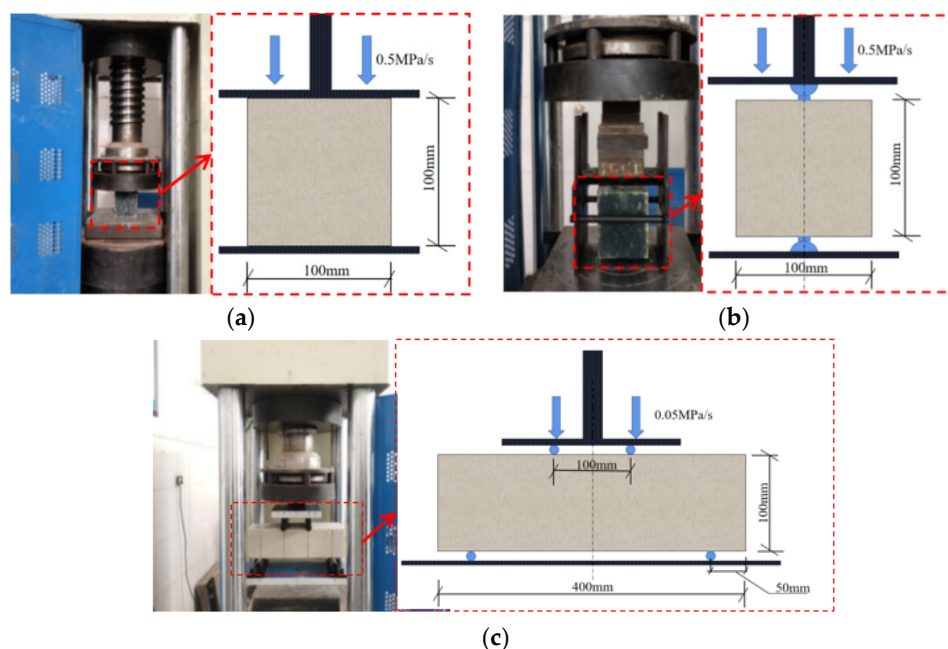


Figure 2. Experimental diagram of mechanical properties: (a) compressive strength experiment; (b) splitting tensile strength experiment; (c) flexural strength experiment.

The softening coefficient and porosity were experimented according to the “Standard Test Method for Density, Absorption, and Porosity of Hardened Concrete” (ASTM C642-13) [41]

and the “Technical Specification for the Application of Aggregate Permeable Concrete” (CJJ/T 253-2016). The relevant calculation formulas are shown in Equations (1)–(3)

$$K = \frac{f_1}{f_0} \quad (1)$$

$$p = \left(1 - \frac{m_0 - m_1}{\rho V}\right) \times 100\% \quad (2)$$

$$\rho_0 = \frac{m_0}{V} \quad (3)$$

where  $K$  is the softening coefficient,  $f_1$  is the compressive strength of the concrete experiment block under the state of water absorption saturation,  $f_0$  is the compressive strength of the concrete experiment block in the air-dried state,  $p$  is the concrete porosity,  $V$  is the volume of the specimen in the dry state,  $m_0$  is the mass of the specimen in the dry state,  $m_1$  is the reading on the tray balance of the specimen in water,  $\rho$  is the density of water, and  $\rho_0$  is the density of water.

The images of the CLC performance test process are shown in the following figures. The slump test process is shown in Figure 3. In the softening coefficient test, the specimen was fully soaked, as shown in Figure 4, and the dry density and porosity test is shown in Figures 5 and 6.



**Figure 3.** Slump of different shell fine aggregate replacement rates.



**Figure 4.** Specimen fully soaked.

In the softening coefficient test, 10 cube test blocks were selected for each group of test blocks. Among them, 5 were immersed in tap water at a temperature of  $20 \pm 5$  °C for 96 h. Then, the specimens were taken out and placed on a wire mesh to drain for 1 min. The excess moisture was then wiped off the surface of the specimen with a wrung wet towel. The other 5 test blocks were placed in a curing room with a temperature of  $20 \pm 5$  °C and a relative humidity of  $50 \pm 15\%$  for 96 h to allow the test pieces to reach an air-dry state.

During the dry density coefficient measurement process, the time settings were as follows. The specimen was placed in an oven at  $105 \pm 5$  °C and baked to a constant weight for 24 h. After taking it out, it was placed at room temperature for cooling. The specimen was then completely immersed in water for 24 h and the slump was measured directly when the specimen was made.



**Figure 5.** Specimen fully drying.



**Figure 6.** Hydrostatical balance.

### 3. Experimental Results

#### 3.1. Effect of Shell Sand on Mechanical Properties

##### 3.1.1. Compressive Strength Growth Trend

Figure 7 shows the averaged compressive strength for each group of specimens at 3, 7, 14 and 28 days. The figure also shows that the compressive strength growth law of each experimental group is the same as the control group. When the content of shell sand is less than 10%, the compressive strength of S-CLC is better than that of CLC, and when the replacement rate of shell sand exceeds 10%, the strength shows a downward trend and is lower than that of the control group. In addition, when the shell sand replacement rate is less than 10%, S-CLC also exhibits early strength properties, which are conducive to the development of on-site construction.

##### 3.1.2. Mechanical Properties Change Trend

The effects of changes in shell sand substitution rate on the 28-day compressive strength, splitting tensile strength and flexural strength of S-CLC are shown in Figure 8. Compared with the control group, with the increase in the shell sand replacement rate (5%, 10%, 15%, 20% and 25%), the compressive strength of S-CLC increased by 6.53%, 3.41%,  $-2.56\%$ ,  $-7.39\%$  and  $-19.03\%$ . The splitting tensile strength increased by 1.70%, 0.42%,  $-1.91\%$ ,  $-5.52\%$  and  $-8.92\%$ , and the flexural strength increased by 3.40%, 1.54%,  $-1.85\%$ ,  $-8.02\%$  and  $-14.81\%$ . The three mechanical properties show the same change trend, and reach the maximum value when the shell sand replacement rate is 5%. By comparing the

conclusions of this paper with those of Kuo [33], Yang [34], Varhen [35] and Ruslan [42] et al., when the replacement rate of shell sand is about 5%, the performance of ordinary concrete and other concrete will reach the optimal value at this time, which indicates that the influence law of shell sand on most concrete is similar. It also proves the accuracy of the experiment.

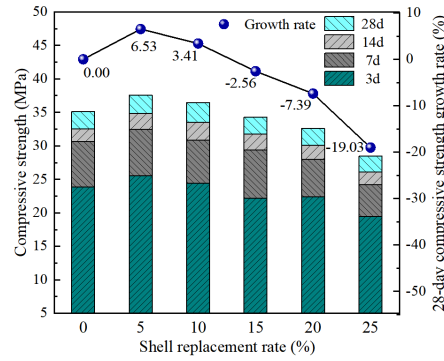


Figure 7. Changes in compressive strength of each group of specimens at different ages.

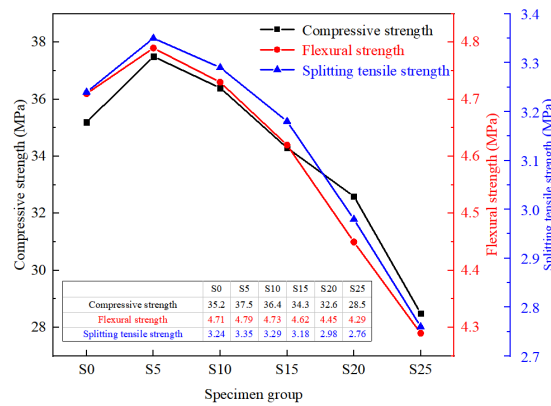


Figure 8. Effect of shell sand replacement rate on mechanical properties.

### 3.1.3. Correlation between Mechanical Properties

From the changing rules of compressive strength, splitting tensile strength and flexural strength as shown in Figure 8, it can be seen that S-CLC have a certain similar relationship with ordinary concrete in terms of mechanical properties. Therefore, this paper relies on ACI363R-92 [43], which is used to describe the properties of ordinary concrete and adjust its related parameters to describe the relationship between S-CLC compressive strength and splitting tensile strength. The fit result is shown in Figure 9a. Similarly, the correlation between compressive strength and fracture strength is described using the model proposed by Jena [44] and Albitar [45]. The results are shown in Figure 9b. The correlation coefficients obtained from the fit results are 0.9793 and 0.9496, which show that the fit effect is excellent. The fit formulas  $f_{ts} = 0.23f_{cu}^{0.74}$  and  $f_t = 1.05f_{cu}^{0.42}$  can fully provide reference and support for scheme design and on-site construction.

### 3.1.4. Relationship between Age and Performance

In order to better describe the relationship between the compressive strength and age of S-CLC and facilitate on-site construction, this paper uses the European specification CEB-FIP Model Code 1990 [46] to describe the relationship between OPC concrete strength growth and age, and uses the S5 group as the research object to find the formula  $f_c(t) = \left(\frac{f_c(7)}{f_c(28)}\right)^{\sqrt{28/t}-1} \times f_c(28)$ , which is also suitable to describe the relationship between S-CLC compressive strength and age. Since there is a strong correlation between splitting

tensile strength, tensile strength and compressive strength, this paper does not give the change laws between them and their age. If necessary, it can be converted according to its relationship with compressive strength.

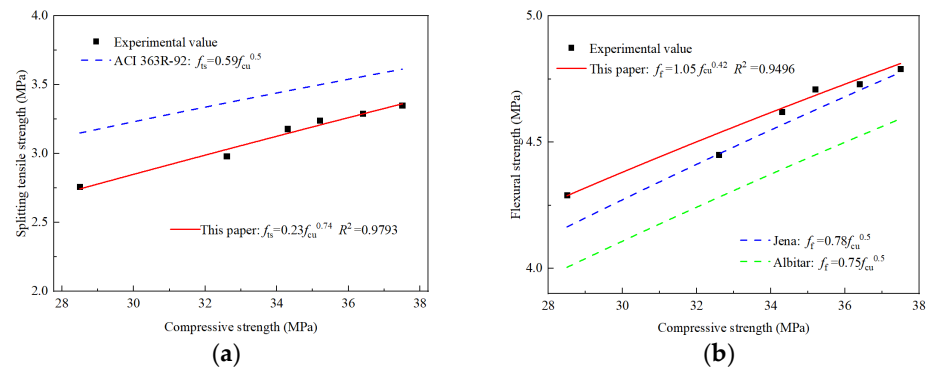


**Figure 9.** The fitted relationship between the mechanical strength: (a) the fitted relationship between compressive strength and splitting tensile strength of S-CLC; (b) the fitted relationship between compressive strength and flexural strength of S-CLC.

### 3.2. Effect of Shell Sand on Working Capability

#### 3.2.1. Softening Coefficient Changes Trend

It was found in the experiment that the replacement rate of shell sand had no significant influence on the coagulation time of CLC. After field records, we found that the initial coagulation time was 28 min and the final coagulation time was 57 min.

It can be seen from the data that the softening coefficient of each group is greater than 0.85, which meets the requirements of ceramsite concrete in a long-term wet or soaked environment. As can be seen from the change trend in Figure 10, the softening coefficient increases first and then decreases with the increase in the replacement rate of shell fine aggregate, the softening coefficient of S-CLC increased by 4.44%, 2.22%, −1.11%, −3.33% and −4.44% when the shell sand replacement rate increased compared with the control group and the softening coefficient of group S5 reaches the highest, which is similar to the effect of the replacement rate of shell fine aggregate on the working performance of ceramics.

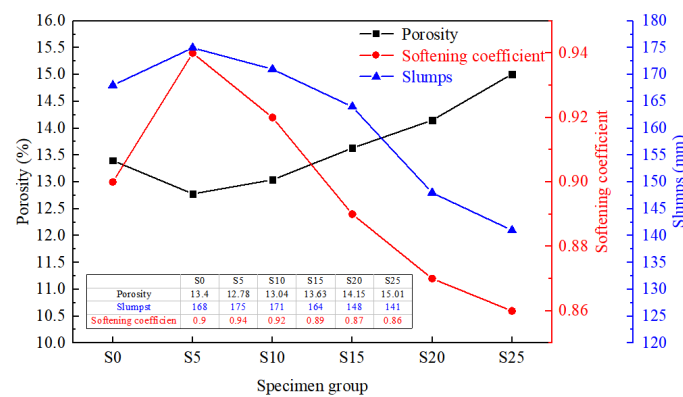


**Figure 10.** Effect of shell sand replacement rate on working capability.

With the increase in the replacement rate of shell fine aggregate, the slump of ceramsite concrete presents the best state in group S5, and the hydration reaction is more adequate, which makes the internal void less, and thus makes the ceramsite concrete lose less compressive strength when it is saturated with water absorption. However, with the increase in the replacement rate of shell fine aggregate, the workability of ceramide concrete is improved. A decrease affects the hydration reaction effect, resulting in more and more

internal voidage of ceramsite concrete, resulting in a greater loss of compressive strength after saturated water absorption.

### 3.2.2. Slump Changes Trend

As can be seen from Figure 10, compared with the control group, as the shell sand content (5%, 10%, 15%, 20%, 25%) increases in S-CLC, the slump increases by 7 mm, 3 mm, −4 mm, −20 mm and −28 mm. The appropriate slump indicates that S-CLC has excellent plasticizing performance and pump ability, and can meet the needs of on-site construction. The slump of ceramsite concrete reached 175 mm when the replacement rate of shell fine aggregate was 5%, which increased by 4.2% compared with that of ceramsite concrete with a zero shell fine aggregate replacement rate. When the replacement rate of shell fine aggregate is 10% or more, the slump of ceramsite concrete shows a decreasing trend, but the slump of ceramsite concrete at a 10% shell replacement rate is still greater than that of a zero shell fine aggregate replacement rate. The main reasons for this phenomenon are that the surface of the shell is smooth, and when a small amount of shell fine aggregate replaces the river sand, the fluidity of the concrete will be promoted, and the slump of the concrete will be increased. However, when the shell is flat, and with the increase in the shell replacement rate, the specific surface area of fine aggregate increases greatly, which increases the friction between the concrete particles and gradually reduces the slump.

### 3.2.3. Porosity Changes Trend

It is worth noting that compared with group S0, when the replacement rate of shell fine aggregate is 5%, the porosity of light aggregate concrete shows a decreasing trend, and the reduction rate reaches 4.63%. However, after that, the porosity of light aggregate concrete gradually increased with the increase in the shell fine aggregate replacement rate, and the porosity of group S25 increased by 17.45% compared with group S5.

Based on this phenomenon, the explanation given in this paper is as follows: considering the influence of the replacement rate of shell fine aggregate on the working performance of light aggregate concrete, compared with the ceramsite concrete with a zero shell replacement rate, the slump of the ceramsite concrete with a 5% shell fine aggregate replacement rate is increased, which also makes the ceramsite concrete more dense and fewer pores occur inside the ceramsite concrete. Compared with river sand, although the porosity of shell is relatively large, its effect on the increase of porosity of light aggregate concrete is not great because of the low replacement rate of shell fine aggregate.

Therefore, this paper uses the Balshin model [47], Ryshkewitch model [48] and Hasselman model [49] to analyze if the relationship curve between the pores and compressive strength was fitted respectively, and the fit results are shown in Figure 11.

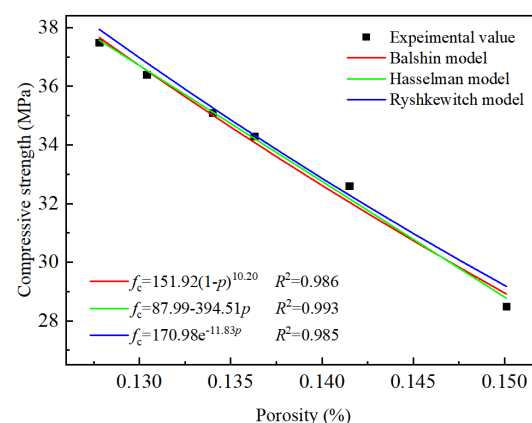


Figure 11. Fitting relationship between porosity and compressive strength.

As shown in Figure 11, the correlations of the four models all exceed 0.985, which shows that porosity has a high degree of impact on mechanical properties, and will be further studied in a subsequent paper.

In summary, as the shell sand content increases, the performance of S-CLC shows a trend of first, an increase and then, a decrease. When the shell sand replacement rate is 5%, all properties reach the optimal value.

### 3.3. Effect of Shell Sand on the Failure Pattern

#### 3.3.1. Compression Failure Interface

During the compression test of alkali-induced lightweight aggregate concrete, the failure process of the specimen was observed. As the load continued to increase, tiny cracks began to appear on the upper and lower surfaces of the specimen, and expanded as the load increased. It can be observed that the cracks on the four sides of the specimen continued to extend toward the middle and the crack width continued to increase, and as the load continued to increase, the cracks continued to increase and the concrete on the surface of the specimen began to peel off and the specimen entered the failure stage.

After the loading was completed, it was observed that the failure shape of the cube specimen was mainly in the shape of an overhead cone. This is because the upper and lower plates of the pressure testing machine constrain the lateral cracking of the upper and lower parts of the specimen, while the middle concrete far away from the upper and lower parts subject to the constraint is small, so it is in the shape of a cone. The fracture form inside the specimen is mainly the fracture of coarse aggregate ceramsite, and there is no damage to the bonding surface of ceramsite and slag. As shown in Figure 12, the failure interface of the specimen becomes more and more obvious in the shape of a cone as the shell sand content increases.



**Figure 12.** Failure interface of the specimen under Compression.

#### 3.3.2. Tension Bending Failure Interface

As shown in Figure 13, when the shell replacement rate increases, more and more exposed shells (circled in the figure) are exposed at the interface. During the loading process of the specimen, a tiny sound of ceramsite breaking can be heard, and as the load continues to increase, tiny cracks begin to appear on the cross section until the specimen splits and fails.

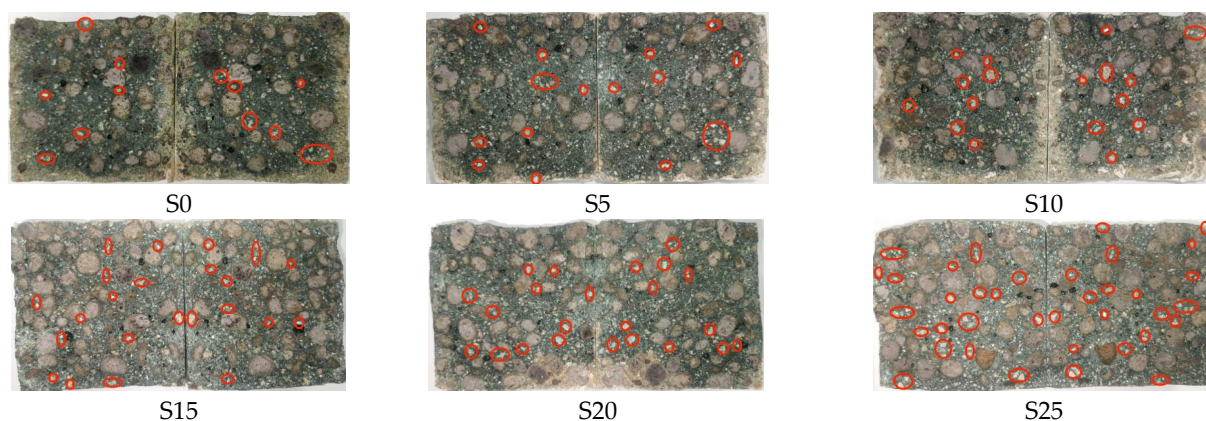


**Figure 13.** Failure interface of the specimen under Tension Bending.

#### 4. Analysis of the Impact of Shell Sand on Performance

##### 4.1. Pore Analysis

In order to explore the impact of internal pores on the performance of S-CLC, this paper used the American Quanta Pore Master 60 GT mercury porosimeter to measure the pore size distribution, most geometric pores and porosity of CLC under different shell sand contents, as shown in Figure 14.



**Figure 14.** American Quanta Pore Master 60 GT mercury porosimeter.

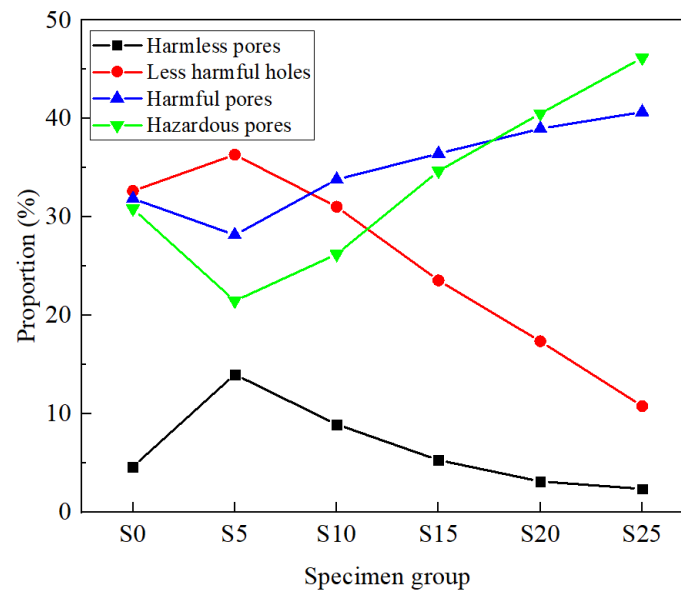
##### 4.1.1. Pore Change Trend

The pore structure characteristic parameters and pore size distribution curve are shown in Table 4. The total porosity, most available pore size, harmful pore and multiple harmful pore of CLC tend to the minimum value when the shell sand replacement rate is 5%. With the increase in the shell sand substitution rate, the harmful holes and multiple harmful holes also increase, and the corresponding harmless holes and less harmful holes decrease.

In order to more intuitively describe the impact of shell sand with different replacement rates on various pores, this paper plots the data obtained in Figure 15. Combined with Table 3, it can be found that with the increase in the shell sand replacement rate, the porosity of S-CLC still showed a trend of gradual increase, and the number of large pores gradually increased while the small pores gradually decreased. This indicates that the presence of excess shell sands will make the structure of S-CLC more loose and the overall mechanical properties will decline.

**Table 4.** Characteristic parameters and pore size distribution of concrete pore structure under different shell sand contents.

| Group | Total Porosity | Maximum Pore Size (nm) | Harmless Pores ( $d \leq 20$ nm) | Less Harmful Holes ( $20 \text{ nm} < d \leq 50$ nm) | Harmful Pores ( $50 \text{ nm} < d \leq 200$ nm) | Hazardous Pores ( $d > 200$ nm) |
|-------|----------------|------------------------|----------------------------------|--|--|---------------------------------|
| S0    | 13.40          | 51.05                  | 4.63                             | 32.66  | 31.86  | 30.85                           |
| S5    | 12.78          | 44.91                  | 14.00                            | 36.33  | 28.19  | 21.48                           |
| S10   | 13.04          | 56.16                  | 8.93                             | 31.04  | 33.82  | 26.21                           |
| S15   | 13.63          | 58.77                  | 5.31                             | 23.56  | 36.45  | 34.68                           |
| S20   | 14.15          | 66.39                  | 3.13                             | 17.37  | 38.98  | 40.52                           |
| S25   | 15.01          | 70.24                  | 2.38                             | 10.78  | 40.68  | 46.16                           |

**Figure 15.** Proportion of different pores in each group of specimens.

#### 4.1.2. Analysis of the Impact of Pore Changes on Performance

When an appropriate amount of shells replace fine aggregate, it can well fill the gaps inside the specimen, making the S-CLC denser and conducive to improving the mechanical properties. The reduction of internal pores results in less compressive strength loss when S-CLC is saturated with water, thereby improving the softening resistance. Since shells are relatively smooth, when a small amount of shell fine aggregate replaces sand, it will promote the fluidity of concrete and increase the slump.

Since the shell sand is mostly flat, the specific surface area of the fine aggregate increases significantly as the shell replacement rate increases, thereby increasing the internal pores of the concrete. The decrease in compactness leads to a decrease in mechanical properties and, at the same time, the internal pores. The increase leads to an increase in the loss of compressive strength after water absorption, which in turn leads to a decrease in its anti-softening coefficient. In addition, flat shell sand increases the friction between concrete particles, resulting in reduced fluidity and lower slump.

#### 4.2. Microelectron Microscopy Analysis

As aforementioned, microstructural analysis is an important means to research the changes and influences mechanisms of concrete properties. For this purpose, this paper uses a field emission scanning electron microscope (SEM) to conduct microscopic analysis of S-CLC by observing the cracks and hydration products in the interface transition zone, which can clarify the microscopic mechanism that causes the performance changes of S-CLC. SEM photos and sample photos are shown in Figures 16 and 17 respectively.

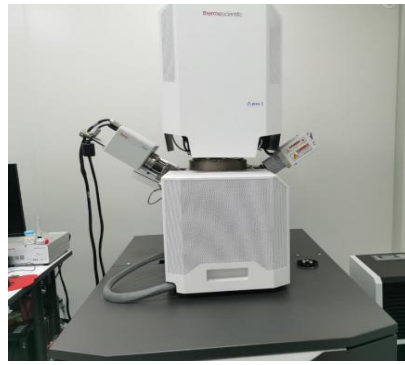


**Figure 16.** Field emission scanning electron microscope (FESEM).

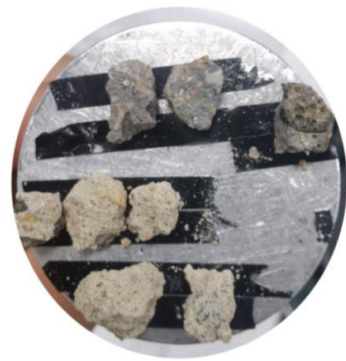


**Figure 17.** Sample stand.

#### 4.2.1. Ceramic Micropore Analysis

When the ceramic particles are enlarged as shown in Figure 18, it can be found that they are covered with honeycomb-shaped irregular micropores. This special structure allows the ceramsite itself to have a certain water storage capacity, which can increase free water to further promote the hydration during the subsequent concrete solidification process. In addition, shell sand contains calcium compounds, which continuously release  $\text{Ca}^{2+}$  during the hydration process [30]. These  $\text{Ca}^{2+}$  react with the hydration products in the slurry, further promoting the hydration reaction, which also explains why S-CLC has a certain early strength.

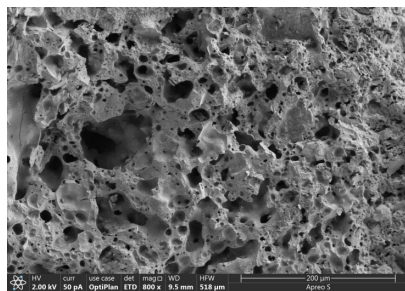


**Figure 18.** Ceramsite surface micrograph (magnified to 800 times).

#### 4.2.2. Analysis of the Interface between Ceramsite and Hydration Products

By observing the enlarged interface between the ceramsite and the hydration product, it can be seen that the bonding surface between the ceramsite and the slag matrix is not a “surface”, but an “area” or “band” with a certain thickness, as shown in Figure 19.

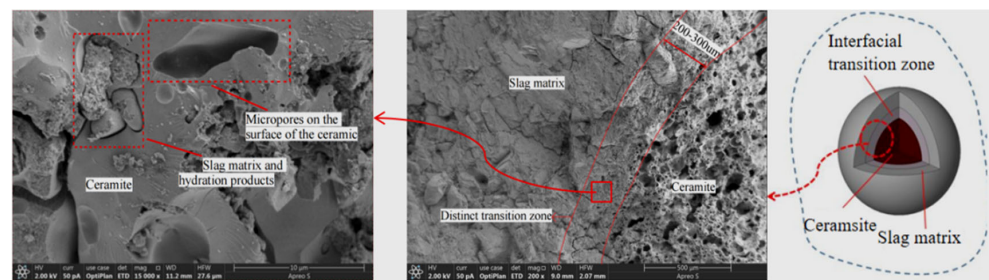


**Figure 19.** Adhesive surface of ceramsite and alkali-activated matrix (magnified to 200–15,000 times).

Further magnifying the joint between ceramsite and hydration products, it can be seen that a large amount of hydration products and unreacted slag are collectively embedded in the micropores of the ceramsite, forming a mortise and tenon structure with a strong mechanical connection ability. The photo of the hydration product embedded in the ceramsite is shown in Figure 20.

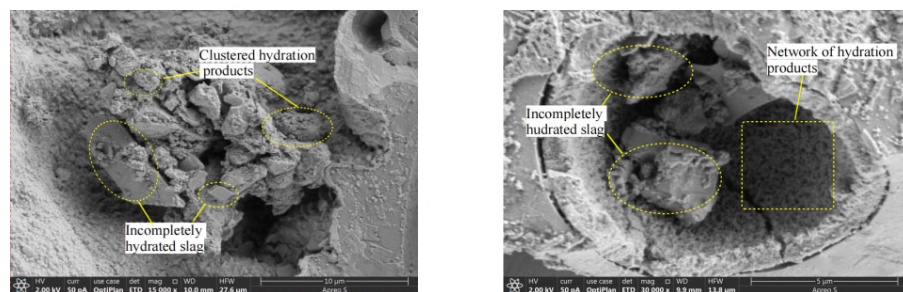


**Figure 20.** Hydration products in ceramsite pores (magnified to 15,000–30,000 times).

#### 4.2.3. Analysis of Specimen Failure Morphology

By observing the shell sand with exposed leakage at the damaged interface, it can be seen that compared with river sand, the inner surface of shell sand is relatively smooth, resulting in poor adhesion between shell sand and hydration products. As can be seen from Figure 21, there is almost no slag base retained on the surface of the shell sand, indicating that the bonding effect between the two is poor, thus forming an interface bonding defect area.

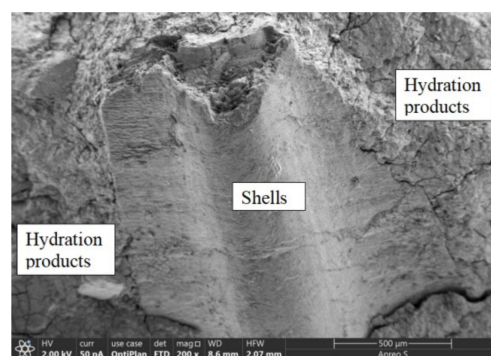


**Figure 21.** Microscopic view of shell sand (magnified to 200 times).

As the shell sand replacement rate increases, the defect area between the shell sand and the slag foundation increases, and the load inside the concrete is mainly borne by the ceramsite. Then, the connection strength of the mortise and tenon structure between the ceramsite, hydration products and unreacted slag is greater than the ceramsite itself. This also explains that the damage to the specimens mentioned above is mostly caused by the

damage of the ceramsite. It also shows that one of the keys to improving the strength of S-CLC is to increase the strength of the ceramsite.

#### 4.2.4. Porosity Analysis at the Microscopic Level

Further analysis of the mechanical properties of ceramsite shell sand lightweight aggregate concrete from a microscopic perspective (as shown in Figure 22) shows that when the shell sand replacement rate is zero, there are gaps at the aggregate interface, the concrete is not dense and there are pores. There are also scattered flakes and flocculated calcium silicate hydrate (C-S-H) gel is discontinuous and not tightly bonded, resulting in poor mechanical properties of concrete. When the shell sand replacement rate is 5%, the concrete has good density, a small amount of dispersed and free flaky C-S-H gel and fine cracks. Excellent density not only improves the mechanical properties of S-CLC but also promotes its resistance to softening.

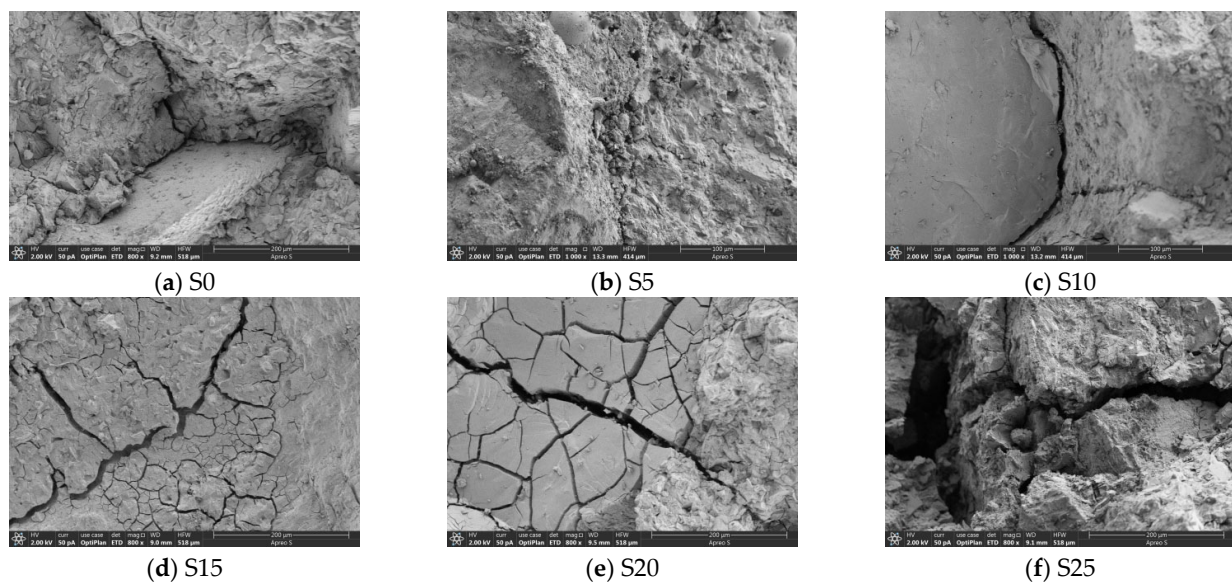


**Figure 22.** Micrograph of test block (magnified to 800–1000 times).

When the shell sand replacement rate exceeds 10%, cracks gradually begin to appear in S-CLC and develop rapidly as the shell sand content increases. Not only does it lead to an increase in the loss of compressive strength after the concrete is saturated with water and loses some of its anti-softening properties, it is also not conducive to the development of mechanical properties.

In addition, microelectron microscopy further verified the shell–sand interface wall effect; that is, the excess shell sand will increase porosity due to its flat shape. It was also found that its planar shape interferes with particle accumulation, reducing the fluidity and slump of concrete.

## 5. Conclusions

This paper draws the following conclusions from studying the impact of shell sand with different replacement rates on the performance of S-CLC:

1. The influence of shell sand on the performance of S-CLC is bidirectional, directly manifested by affecting the porosity. When the replacement rate of shell sand is less than 5%, it can reduce the generation of various harmful pores inside the concrete. However, when it exceeds this value, the effect will be the opposite.
2. When the substitution rate of shell sand is 5%, S-CLC has the highest compressive strength, splitting tensile strength and flexural strength, reaching 37.5 MPa, 3.24 MPa and 4.79 MPa, respectively. In terms of working performance, slump is 175 mm,

- porosity reaches the minimum value of 12.78% and the anti-softening coefficient is 0.94.
3. The various micropores of the ceramsite itself can store a small amount of free water and promote the subsequent hydration process, giving S-CLC a certain early strength. Various hydration products and unreacted slag matrix will also be embedded in these micropores, forming a mortise and tenon structure with high connection strength.
  4. The inner surface of the shell sand is too smooth, which makes the bonding strength between the shell sand and the hydration product weak, forming a bonding defect area. In addition, the strength of the ceramsite itself is lower than the bonding strength with the hydration products and slag matrix, so the stress damage of the specimen is mostly caused by the damage of the ceramsite.
  5. According to the above analysis of the “defect area” of the shell sand connection, the special “mortise and tenon structure” between the ceramic particle and the gelled product and the fracture morphology of the interface of the specimen, it can be seen that appropriately increasing the strength of the ceramic particle itself may improve the overall mechanical properties of S-CLC. Therefore, it can be used in non-key load-bearing parts of building structures. In addition, S-CLC also has good thermal insulation performance and corrosion resistance, making it a good application environment.

**Author Contributions:** D.L.: Conceptualization, Data curation, Formal analysis, Writing—original draft, Writing—review & editing. S.L.: Data curation, Formal analysis, Writing—review & editing. H.L.: Data curation, Formal analysis, Writing—review & editing. Q.W.: Conceptualization, Funding acquisition, Writing—review & editing. All authors have read and agreed to the published version of the manuscript.

**Funding:** This research received no external funding.

**Data Availability Statement:** The original contributions presented in the study are included in the article, further inquiries can be directed to the corresponding author.

**Conflicts of Interest:** Author Hengxuan Lun was employed by the company China Construction Eighth Bureau First Construction Co., Ltd. The remaining authors declare that the research was conducted in the absence of any commercial or financial relationships that could be construed as a potential conflict of interest.

## References

1. Behera, M.; Bhattacharyya, S.; Minocha, A.; Deoliya, R.; Maiti, S. Recycled aggregate from C&D waste & its use in concrete—A breakthrough towards sustainability in construction sector: A review. *Constr. Build. Mater.* **2014**, *68*, 501–516. [\[CrossRef\]](#)
2. Scrivener, K.L.; Kirkpatrick, R.J. Innovation in use and research on cementitious material. *Cem. Concr. Res.* **2008**, *38*, 128–136. [\[CrossRef\]](#)
3. Li, X.G.; Yan, F.J.; Yue, X.T.; Wang, X.G. Research progress of ceramsite concrete. *Bull. Chin. Ceram. Soc.* **2020**, *39*, 3407–3418+3452.
4. Li, Z.; Fei, M.-E.; Huyan, C.; Shi, X. Nano-engineered, Fly Ash-Based Geopolymer Composites: An Overview. *Resour. Conserv. Recycl.* **2020**, *168*, 105334. [\[CrossRef\]](#)
5. Provis, J.L.; Bernal, S.A. Geopolymers and Related Alkali-Activated Materials. *Annu. Rev. Mater. Res.* **2014**, *44*, 299–327. [\[CrossRef\]](#)
6. Eziefula, U.G.; Ezech, J.C.; Eziefula, B.I. Properties of seashell aggregate concrete: A review. *Constr. Build. Mater.* **2018**, *192*, 287–300. [\[CrossRef\]](#)
7. Zhang, Y.S.; Sun, W.; Li, J.Z. Hydration process of interfacial transition in potassium polysialate (K-PSDS) geopolymer concrete. *Mag. Concr. Res.* **2005**, *57*, 33–38. [\[CrossRef\]](#)
8. Peng, X.Q.; Yang, T.; Wang, K.Y.; Meng, X. Preparation of Geopolymeric Concrete and Its Application to Rapid Repair of Cement Concrete Pavement. *J. Southwest Jiaotong Univ.* **2011**, *46*, 205–210.
9. Van Deventer, J.S.; Provis, J.L.; Duxson, P. Technical and commercial progress in the adoption of geopolymer cement. *Miner. Eng.* **2012**, *29*, 89–104. [\[CrossRef\]](#)
10. Nuruddin, M.F.; Kusbiantoro, A.; Qazi, S.; Shafiq, N. Compressive strength and interfacial transition zone characteristic of geopolymer concrete with different cast in-situ curing condition. *World Acad. Sci. Eng. Technol. WASET* **2011**, 25–28.
11. Lloyd, R.R.; Provis, J.L.; van Deventer, J.S.J. Acid resistance of inorganic polymer binders. 1. Corrosion rate. *Mater. Struct.* **2011**, *45*, 1–14. [\[CrossRef\]](#)

12. Bernal, S.A.; Provis, J.L.; Walkley, B.; San Nicolas, R.; Gehman, J.D.; Brice, D.G.; Kilcullen, A.R.; Duxson, P.; Van Deventer, J.S. Gel nanostructure in alkali-activated binders based on slag and fly ash, and effects of accelerated carbonation. *Cem. Concr. Res.* **2013**, *53*, 127–144. [[CrossRef](#)]
13. Puertas, F.; Palacios, M.; Manzano, H.; Dolado, J.S.; Rico, A.; Rodríguez, J. A model for the C-A-S-H gel formed in alkali-activated slag cements. *J. Eur. Ceram. Soc.* **2011**, *31*, 2043–2056. [[CrossRef](#)]
14. Fernández-Jiménez, A.; Palomo, A.; Criado, M. Microstructure development of alkali-activated fly ash cement: A descriptive model. *Cem. Concr. Res.* **2005**, *35*, 1204–1209. [[CrossRef](#)]
15. Zhang, Y.; Xiao, R.; Jiang, X.; Li, W.; Zhu, X.; Huang, B. Effect of particle size and curing temperature on mechanical and microstructural properties of waste glass-slag-based and waste glass-fly ash-based geopolymers. *J. Clean. Prod.* **2020**, *273*, 122970. [[CrossRef](#)]
16. Cao, Y.; Wang, Y.; Zhang, Z.; Ma, Y.; Wang, H. Recent progress of utilization of activated kaolinitic clay in cementitious construction materials. *Compos. Part B Eng.* **2021**, *211*, 108636. [[CrossRef](#)]
17. Dai, X.; Ren, Q.; Aydin, S.; Yardimci, M.Y.; De Schutter, G. Accelerating the reaction process of sodium carbonate-activated slag mixtures with the incorporation of a small addition of sodium hydroxide/sodium silicate. *Cem. Concr. Compos.* **2023**, *141*, 105118. [[CrossRef](#)]
18. Wang, S.-D.; Scrivener, K.L. Hydration products of alkali activated slag cement. *Cem. Concr. Res.* **1995**, *25*, 561–571. [[CrossRef](#)]
19. Feng, D.; Wang, J.; Wang, Y.; Liang, S. Experimental study on solidification/stabilisation of high-salt sludge by alkali-activated GGBS and MSWI bottom ash cementitious materials. *Case Stud. Constr. Mater.* **2023**, *19*, e02417. [[CrossRef](#)]
20. Su, C.; Zhang, J.; Ding, Y. Research on reactivity evaluation and micro-mechanism of various solid waste powders for alkali-activated cementitious materials. *Constr. Build. Mater.* **2024**, *411*, 134374. [[CrossRef](#)]
21. Jeon, I.K.; Azzam, A.; Al Jebaei, H.; Kim, Y.-R.; Aryal, A.; Baltazar, J.-C. Effects of alkali-activated slag binder and shape-stabilized phase change material on thermal and mechanical characteristics and environmental impact of cementitious composite for building envelopes. *J. Build. Eng.* **2023**, *76*, 107296. [[CrossRef](#)]
22. Çelik, A.İ.; Tunç, U.; Bahrami, A.; Karalar, M.; Mydin, M.A.O.; Alomayri, T.; Özkılıç, Y.O. Use of waste glass powder toward more sustainable geopolymer concrete. *J. Mater. Res. Technol.* **2023**, *24*, 8533–8546. [[CrossRef](#)]
23. Meskhi, B.; Beskopylny, A.N.; Stel'makh, S.A.; Shcherban', E.M.; Mailyan, L.R.; Shilov, A.A.; El'shaeva, D.; Shilova, K.; Karalar, M.; Aksoylu, C.; et al. Analytical Review of Geopolymer Concrete: Retrospective and Current Issues. *Materials* **2023**, *16*, 3792. [[CrossRef](#)] [[PubMed](#)]
24. Çelik, A.İ.; Özkılıç, Y.O.; Bahrami, A.; Hakeem, I.Y. Effects of glass fiber on recycled fly ash and basalt powder based geopolymer concrete. *Case Stud. Constr. Mater.* **2023**, *19*, e02659. [[CrossRef](#)]
25. Çelik, A.İ.; Özkılıç, Y.O.; Bahrami, A.; Hakeem, I.Y. Mechanical performance of geopolymer concrete with micro silica fume and waste steel lathe scraps. *Case Stud. Constr. Mater.* **2023**, *19*, e02548. [[CrossRef](#)]
26. Acar, M.C.; Çelik, A.I.; Kayabaşı, R.; Şener, A.; Özdöner, N.; Özkılıç, Y.O. Production of perlite-based-aerated geopolymer using hydrogen peroxide as eco-friendly material for energy-efficient buildings. *J. Mater. Res. Technol.* **2023**, *24*, 81–99. [[CrossRef](#)]
27. Özkılıç, Y.O.; Çelik, A.I.; Tunç, U.; Karalar, M.; Deifalla, A.; Alomayri, T.; Althoey, F. The use of crushed recycled glass for alkali activated fly ash based geopolymer concrete and prediction of its capacity. *J. Mater. Res. Technol.* **2023**, *24*, 8267–8281. [[CrossRef](#)]
28. Olivia, M.; Mifshella, A.A.; Darmayanti, L. Mechanical Properties of Seashell sand Concrete. *Procedia Eng.* **2015**, *125*, 760–764. [[CrossRef](#)]
29. Bamigboye, G.O.; Nworgu, A.T.; Odetoyan, A.O.; Kareem, M.; Enabulele, D.O.; Bassey, D.E. Sustainable use of seashells as binder in concrete production: Prospect and challenges. *J. Build. Eng.* **2020**, *34*, 101864. [[CrossRef](#)]
30. Ismail, I.; Bernal, S.A.; Provis, J.L.; San Nicolas, R.; Hamdan, S.; van Deventer, J.S.J. Modification of phase evolution in alkali-activated blast furnace slag by the incorporation of fly ash. *Cem. Concr. Compos.* **2014**, *45*, 125–135. [[CrossRef](#)]
31. Hasnaoui, A.; Bourguiba, A.; Sebaibi, N.; Boutouil, M. Valorization of queen scallop shell sands in the preparation of metakaolin-based geopolymer mortars. *J. Build. Eng.* **2022**, *53*, 104578. [[CrossRef](#)]
32. Maglad, A.M.; Mydin, A.O.; Datta, S.D.; Tayeh, B.A. Assessing the mechanical, durability, thermal and microstructural properties of sea shell ash based lightweight foamed concrete. *Constr. Build. Mater.* **2023**, *402*, 133018. [[CrossRef](#)]
33. Kuo, W.-T.; Wang, H.-Y.; Shu, C.-Y.; Su, D.-S. Engineering properties of controlled low-strength materials containing waste oyster shells. *Constr. Build. Mater.* **2013**, *46*, 128–133. [[CrossRef](#)]
34. Yang, E.-I.; Yi, S.-T.; Leem, Y.-M. Effect of oyster shell substituted for fine aggregate on concrete characteristics: Part I. Fundamental properties. *Cem. Concr. Res.* **2005**, *35*, 2175–2182. [[CrossRef](#)]
35. Varhen, C.; Carrillo, S.; Ruiz, G. Experimental investigation of Peruvian scallop used as fine aggregate in concrete. *Constr. Build. Mater.* **2017**, *136*, 533–540. [[CrossRef](#)]
36. Zhou, J.; Kang, T.; Wang, F. Pore structure and strength of waste fiber recycled concrete. *J. Eng. Fibers Fabr.* **2019**, *14*. [[CrossRef](#)]
37. Chen, R.X.; Ma, S.; Liu, J.P. Relationship between chloride migration coefficient and pore structures of long-term water curing concrete. *Constr. Build. Mater.* **2022**, *341*, 127741.
38. Tang, M.; Wang, J.C.; Li, L.J. Research on Fractal Characteristics of Concrete Material Pores with MIP. *J. Shenyang Arch. Civ. Eng. Univ. Nat. Sci.* **2001**, 272–275.
39. Zhang, B.; Tan, H.; Shen, W.; Xu, G.; Ma, B.; Ji, X. Nano-silica and silica fume modified cement mortar used as Surface Protection Material to enhance the impermeability. *Cem. Concr. Compos.* **2018**, *92*, 7–17. [[CrossRef](#)]

40. Mehta, P.K. Pore size distribution and permeability of hardened cement pastes. In Proceedings of the 7th International Congress on Cement Chemistry, Paris, France, 30 June–4 July 1980; pp. VII–1–VII–5.
41. *ASTM C642*; Standard Test Method for Density, Absorption, and Voids in Hardened Concrete. ASTM International: West Conshohocken, PA, USA, 2013.
42. Ruslan, H.N.; Muthusamy, K.; Ariffin, N.F.; Wahab, M.M.A.; Mohamad, N. Effect of crushed cockle shell as partial fine aggregate replacement on workability and strength of lightweight concrete. *Mater. Today Proc.* **2021**, *48*, 1826–1830. [[CrossRef](#)]
43. Russell, H.G.; Anderson, A.R.; Banning, J.O.; Cantor, I.G.; Carrasquillo, R.L.; Cook, J.E.; Frantz, G.C.; Hester, W.T.; Saucier, K.L.; Aitcin, P.C.; et al. State-of-the-art report on high-strength concrete. *ACI Comm.* **1997**, *363*, 92.
44. Jena, S.; Panigrahi, R. Performance assessment of geopolymer concrete with partial replacement of ferrochrome slag as coarse aggregate. *Constr. Build. Mater.* **2019**, *220*, 525–537. [[CrossRef](#)]
45. Albitar, M.; Visintin, P.; Ali, M.S.M.; Drechsler, M. Assessing behaviour of fresh and hardened geopolymer concrete mixed with class-F fly ash. *KSCE J. Civ. Eng.* **2014**, *19*, 1445–1455. [[CrossRef](#)]
46. *CEB-FIP Model Code 1990*; Design of Concrete Structures. British Standard Institution: London, UK, 1993.
47. Balshin, M.Y. Relation of mechanical properties of powder metals and their porosity and the ultimate properties of porous metal-ceramic materials. *Dokl. Akad. Nauk. SSSR* **1949**, *67*, 831–834.
48. Ryshkewitch, E. Compression Strength of Porous Sintered Alumina and Zirconia. *J. Am. Ceram. Soc.* **1953**, *36*, 65–68. [[CrossRef](#)]
49. Hasselman, D.P.H.; Fulrath, R.M. Effect of Small Fraction of Spherical Porosity on Elastic Moduli of Glass. *J. Am. Ceram. Soc.* **1964**, *47*, 52–53. [[CrossRef](#)]

**Disclaimer/Publisher’s Note:** The statements, opinions and data contained in all publications are solely those of the individual author(s) and contributor(s) and not of MDPI and/or the editor(s). MDPI and/or the editor(s) disclaim responsibility for any injury to people or property resulting from any ideas, methods, instructions or products referred to in the content.